Anisotropic Magnetoresistance Components in (Ga,Mn)As

A. W. Rushforth,[1] K. Výborný,[2] C. S. King,[1] K. W. Edmonds,[1] R. P. Campion,[1] C. T. Foxon,[1] J. Wunderlich,[3] A. C. Irvine,[4] P. Vašek,[2] V. Novák,[2] K. Olejník,[2] Jairo Sinova,[5] T. Jungwirth,[2,1] and B. L. Gallagher[1]

[1]*School of Physics and Astronomy, University of Nottingham, Nottingham NG7 2RD, United Kingdom*
[2]*Institute of Physics ASCR, Cukrovarnická 10, 162 53 Praha 6, Czech Republic*
[3]*Hitachi Cambridge Laboratory, Cambridge CB3 0HE, United Kingdom*
[4]*Microelectronics Research Centre, Cavendish Laboratory, University of Cambridge, CB3 0HE, United Kingdom*
[5]*Department of Physics, Texas A&M University, College Station, Texas 77843-4242, USA*

(Received 15 February 2007; published 3 October 2007)

We explore the basic physical origins of the noncrystalline and crystalline components of the anisotropic magnetoresistance (AMR) in (Ga,Mn)As. The sign of the noncrystalline AMR is found to be determined by the form of spin-orbit coupling in the host band and by the relative strengths of the nonmagnetic and magnetic contributions to the Mn impurity potential. We develop experimental methods yielding directly the noncrystalline and crystalline AMR components which are then analyzed independently. We report the observation of an AMR dominated by a large uniaxial crystalline component and show that AMR can be modified by local strain relaxation. Generic implications of our findings for other dilute moment systems are discussed.

DOI: 10.1103/PhysRevLett.99.147207 PACS numbers: 75.47.−m, 75.50.Pp, 75.70.Ak

Anisotropic magnetoresistance (AMR) is a response of carriers in magnetic materials to changes of the magnetization orientation. Despite its importance in magnetic recording technologies, the understanding of the microscopic physics of this spin-orbit (SO) coupling induced effect is relatively poor. Phenomenologically, AMR has a noncrystalline component, arising from the lower symmetry for a specific current direction, and crystalline components arising from the crystal symmetries [1,2]. In ferromagnetic metals, values for these coefficients can be obtained by numerical *ab initio* transport calculations [3], but these have no clear connection to the standard physical model of transport arising from spin dependent scattering of current carrying low mass *s* states into heavy-mass *d* states [4]. Experimentally, the noncrystalline and, the typically much weaker, crystalline AMR components in metals have been indirectly extracted from fitting the total AMR angular dependences [2].

Among the remarkable AMR features of (Ga,Mn)As ferromagnetic semiconductors are the opposite sign of the noncrystalline component (compared to most metal ferromagnets) and the crystalline terms reflecting the rich magnetocrystalline anisotropies [5–11]. Microscopic numerical simulations [6,12] consistently describe the sign and magnitudes of the noncrystalline AMR and capture the more subtle crystalline terms associated with, e.g., growth-induced strain [8,12]. As in metals, however, the basic microscopic physics of the AMR still needs to be elucidated, which is the aim of the work presented here.

Theoretically, we separate the noncrystalline and crystalline components by turning off and on band warping and match numerical microscopic simulations with model analytical results. This provides the physical interpretation of the origin of AMR, and of the sign of the noncrystalline term, in particular. Experimentally, we obtain direct and independent access to the noncrystalline and crystalline AMR components using Hall bars fabricated along the principal crystalline axes and Corbino disk samples. We observe unique behavior in ultrathin low-conductive (Ga,Mn)As layers, which show a large, uniaxial crystalline component dominated AMR. Finally, we demonstrate how crystalline AMR components can be strongly modified by local strain relaxation [13].

The experimental data presented in this Letter were measured in compressively strained 25 and 5 nm $Ga_{0.95}Mn_{0.05}As$ films grown by low temperature molecular beam epitaxy on GaAs [001] substrates. Optical lithography was used to fabricate Hall bars aligned along the [100], [010], [110], and $[1\bar{1}0]$ directions, of width 45 μm with voltage probes separated by 285 μm and Corbino disks of inner (outer) diameter 800 μm (1400 μm) in which current flows radially in the plane of the material. Electron beam lithography was used to fabricate 1 μm wide Hall bars in a 25 nm $Ga_{0.95}Mn_{0.05}As$ film. All magnetoresistances were measured with a saturating magnetic field of 1 T applied in the plane of the film, i.e., in the pure AMR geometry with zero (antisymmetric) Hall signal.

The phenomenological decomposition of the AMR of (Ga,Mn)As into various terms allowed by symmetry is obtained by extending the standard phenomenology [1], to systems with cubic [100] plus uniaxial [110] anisotropy. With this we write the longitudinal AMR as, $\Delta\rho_{xx}/\rho_{\mathrm{av}} = C_I \cos 2\phi + C_U \cos 2\psi + C_C \cos 4\psi + C_{I,C} \cos(4\psi - 2\phi)$, where $\Delta\rho_{xx} = \rho_{xx} - \rho_{\mathrm{av}}$, ρ_{av} is the ρ_{xx} averaged over 360° in the plane of the film, ϕ is the angle between the magnetization unit vector $\hat{\mathbf{M}}$ and the current $\mathbf{I}$, and ψ the angle between $\hat{\mathbf{M}}$ and the [110] crystal direction. The four contributions are the noncrystalline term, the lowest order

uniaxial and cubic crystalline terms, and a crossed noncrystalline/crystalline term. The purely crystalline terms are excluded by symmetry for the transverse AMR and we obtain, $\Delta\rho_{xy}/\rho_{\rm av} = C_I \sin 2\phi - C_{I,C}\sin(4\psi - 2\phi)$.

Microscopically, we describe the AMR components starting from the valence-band kinetic-exchange model of (Ga,Mn)As with metallic conductivities, which is an established qualitative and often semiquantitative theoretical approach [14,15]. The description is based on the canonical Schrieffer-Wolff transformation of the Anderson Hamiltonian which for (Ga,Mn)As replaces hybridization of Mn d orbitals with As and Ga sp orbitals by an effective spin-spin interaction of $L = 0, S = 5/2$ local moments with host valence-band states. These states, which carry all the SO coupling, can be described by the $\mathbf{k}\cdot\mathbf{p}$ Kohn-Luttinger Hamiltonian [14,16].

In these dilute moment systems two distinct microscopic mechanisms lead to anisotropic carrier lifetimes [Fig. 1(a)]: One combines the SO coupling in the carrier band with polarization of randomly distributed magnetic scatterers and the other with polarization of the carrier band itself resulting in an asymmetric band-spin texture. Although acting simultaneously in real systems, theoretically we can turn both mechanisms on and off independently. We find that the former mechanism clearly dominates in (Ga,Mn)As which allows us to neglect spin-splitting of the valence band in the following qualitative discussion. This is further simplified by focusing on the noncrystalline AMR in the heavy-hole Fermi surfaces in the spherical, $\mathbf{s} \parallel \mathbf{k}$, spin-texture approximation [17] [see Fig. 1(a)] and considering scattering off a δ-function potential $\propto (\alpha + \hat{\mathbf{M}}\cdot\mathbf{s})$. Here, $\mathbf{s}$ and $\mathbf{k}$ are the carrier spin operator and wave vector, and α represents the ratio of nonmagnetic and magnetic parts of the impurity potential. Assuming a proportionality between conductivity and lifetimes of carriers with $\mathbf{k}||\mathbf{I}$ we obtain,

$$\sigma_{\hat{\mathbf{M}}\parallel\mathbf{I}}/\sigma_{\hat{\mathbf{M}}\perp\mathbf{I}} = (\alpha^2 + 1/4)(\alpha^2 + 1/12)/(\alpha^2 - 1/4)^2. \quad (1)$$

Therefore, when $\alpha \ll 1$, one expects $\sigma_{\hat{\mathbf{M}}\parallel I} < \sigma_{\hat{\mathbf{M}}\perp I}$ (as is usually observed in metallic ferromagnets). The sign of the noncrystalline AMR reverses at a relatively weak nonmagnetic potential ($\alpha = 1/\sqrt{20}$ in the model), its magnitude is then maximized when the two terms are comparable ($\alpha = 1/2$), and, for this mechanism, it vanishes when the magnetic term is much weaker than the nonmagnetic term ($\alpha \to \infty$).

Physically, carriers moving along $\hat{\mathbf{M}}$, i.e., with $\mathbf{s}$ parallel or antiparallel to $\hat{\mathbf{M}}$, experience the strongest scattering potential among all Fermi surface states when $\alpha = 0$, giving $\sigma_{\hat{\mathbf{M}}\parallel I} < \sigma_{\hat{\mathbf{M}}\perp I}$. When the nonmagnetic potential is present, however, it can more efficiently cancel the magnetic term for carriers moving along $\hat{\mathbf{M}}$, and for relatively small α the sign of AMR flips. Since $\alpha < 1/\sqrt{20}$ is unrealistic for the magnetic acceptor Mn in GaAs [12,14] we obtain $\sigma_{\hat{\mathbf{M}}\parallel I} > \sigma_{\hat{\mathbf{M}}\perp I}$, consistent with experiment. Our analysis also predicts that when the SO coupling in the host band is of the form $\mathbf{s} \perp \mathbf{k}$, as in the Rashba-type 2D systems, or when Mn forms an isovalent pure magnetic impurity, e.g., in II-VI semiconductors, the sign of the noncrystalline AMR will be reversed.

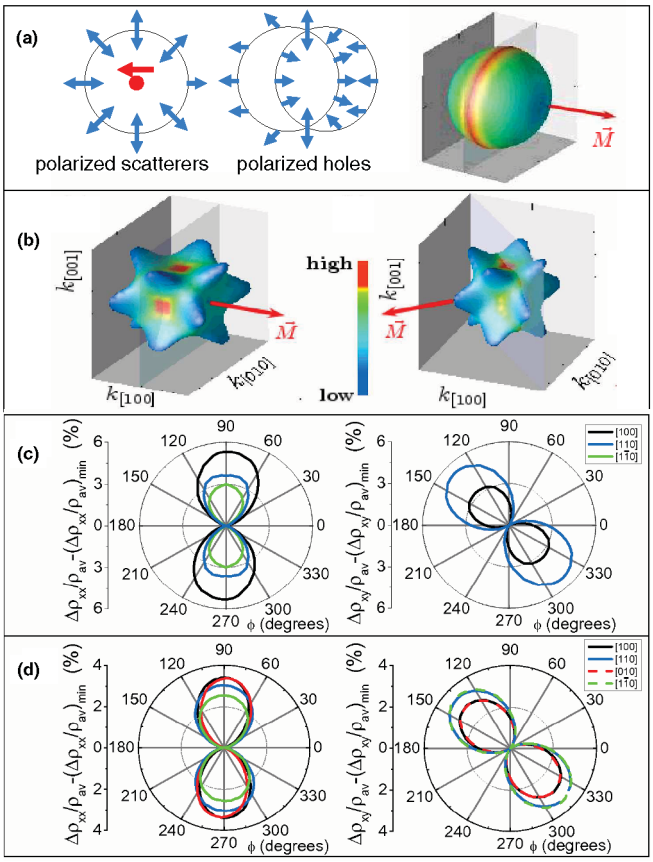

FIG. 1 (color). (a) Noncrystalline AMR in spherical bands: 2D cartoons of AMR mechanisms and calculated anisotropic scattering rate on the 3D Fermi surface of the minority heavy-hole band in $Ga_{0.95}Mn_{0.05}As$. (b) Noncrystalline and crystalline AMR on warped bands: calculated anisotropic scattering rates for $\hat{\mathbf{M}} \parallel$ [100] and [110] axes. (c) Calculated and (d) measured (at 4.2 K) longitudinal and transverse AMR for $Ga_{0.95}Mn_{0.05}As$ as a function of the angle between $\hat{\mathbf{M}}$ and $\mathbf{I}$. The legend shows the direction of the current. The y axes show $\Delta\rho/\rho_{\rm av}$ shifted so that the minimum is at zero.

Numerical simulations of hole scattering rates, illustrated in Fig. 1(a) on a color-coded minority heavy-hole Fermi surface, were obtained within the spherical approximation but including the hole spin polarization, light-hole, and split-off valence bands, and realistic nonmagnetic and magnetic Mn impurity potentials [12]. The simulations confirm the qualitative validity of the analytical, noncrystalline AMR expressions of Eq. (1). The additional crystalline AMR terms are obtained when the spherical approximation is relaxed and band warping is included in

the Kohn-Luttinger Hamiltonian [14,16]. The enhanced scattering of holes moving perpendicular to $\hat{\mathbf{M}}$ seen in Fig. 1(b) reflects the persistence of a strong noncrystalline component in the warped bands. The presence of the crystalline components in these anisotropic Fermi surfaces is also clearly apparent in Fig. 1(b). In (Ga,Mn)As, the crystalline terms reflect the biaxial cubic anisotropy of these zincblende compounds combined with a [110] uniaxial component [18].

We conclude the theory discussion by showing in Fig. 1(c) full numerical Boltzmann theory simulations of the AMR for a weakly (15%) compensated $Ga_{0.95}Mn_{0.05}As$ material. The noncrystalline AMR contributes strongly and, as explained above, leads to a higher resistance state for $\mathbf{I} \perp \hat{\mathbf{M}}$. Differences among AMRs for current along the [100], [110], and $[1\bar{1}0]$ directions show that cubic and uniaxial crystalline terms are also sizable. This phenomenology is systematically observed in experimental AMRs of weakly or moderately compensated metallic (Ga,Mn)As films. Typical data for such systems, represented by the 25 nm $Ga_{0.95}Mn_{0.05}As$ film with 3.6% AMR, are shown in Fig. 1(d) for Hall bars patterned along different crystallographic directions.

Above we have shown that diluted magnetic semiconductors like (Ga,Mn)As allow us to formulate the theory of AMR from the understanding of the very basic microscopic mechanisms. In what follows we focus on several unique experimental aspects of the AMR in these systems. The high crystalline quality and metallic character of the samples allow us to produce low contact resistance Hall bars accurately orientated along the principal crystallographic axes, from which it is possible to extract the independent contributions to the AMR. We are also able to fabricate low contact resistance Corbino disk samples for which the averaging over the radial current lines eliminates all effects originating from a specific direction of the current. Corbino measurements are possible in these materials because they are near perfect single crystals but with low carrier density and mobility (compared with single crystal metals) and so can have source-drain resistances large compared with the contact resistances.

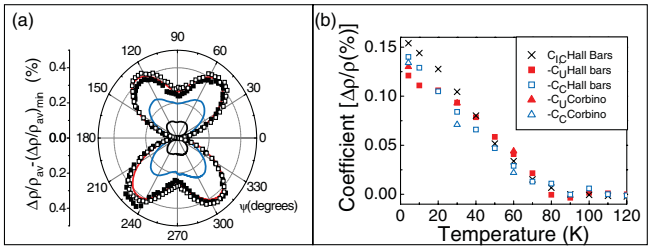

FIG. 2 (color). (a) AMR of the 25 nm $Ga_{0.95}Mn_{0.05}As$ film in the Corbino geometry at 4.2 (red line), 30 (blue line), and 60 K (black line) and the crystalline component extracted from the Hall bars (AMR[110] + AMR[$1\bar{1}0$])/2 (closed points) and (AMR[100] + AMR[010])/2 (open points). (b) Temperature dependence of the crystalline terms extracted from the Hall bars and Corbino devices.

Measured results for a Corbino device fabricated from the same 25 nm $Ga_{0.95}Mn_{0.05}As$ film as used for the Hall bars are shown in Fig. 2(a). The AMR signal is an order of magnitude weaker than in the Hall bars and is clearly composed of a uniaxial and a cubic contribution. Figure 2(a) also shows the crystalline components of the AMR extracted by fitting the Hall bar data to the phenomenological longitudinal and transverse AMR expressions [20]. Figure 2(b) shows the consistency for the coefficients $C_{I,C}$, C_U, and C_C when extracted from the Hall bar and Corbino disk data over the whole range up to the Curie temperature (80 K). Note that the uniaxial crystalline term, C_U, becomes the dominant term for $T \geq 30$ K. This correlates with the uniaxial component of the magnetic anisotropy which dominates for $T \geq 30$ K as observed by SQUID magnetometry measurements (not shown). Our work shows that in (Ga,Mn)As ferromagnets, the symmetry breaking mechanism behind the previously reported [19] uniaxial magnetocrystalline anisotropy in the magnetization also contributes to the AMR.

We now discuss the unique AMR phenomenology observed on ultrathin (5 nm) $Ga_{0.95}Mn_{0.05}As$ films. Measurements on the Hall bars in Fig. 3(a) show that the AMR is very different from that observed in the 25 nm film. Application of the phenomenological analysis to the Hall bar data shows that the crystalline terms dominate the AMR with the uniaxial crystalline term being the largest. SQUID magnetometry on 5 nm $Ga_{0.95}Mn_{0.05}As$ films consistently shows that the uniaxial component of the magnetic anisotropy dominates over the whole temperature range [21]. The Corbino disk AMR data for a nominally identical 5 nm film, shown in Fig. 3(b), confirm our ob-

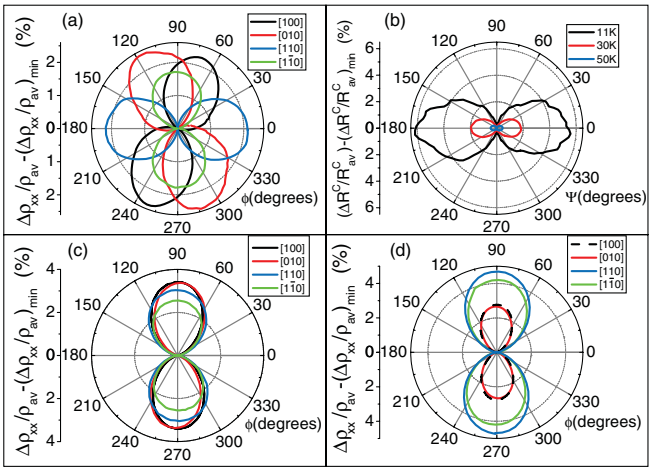

FIG. 3 (color). Longitudinal AMR of the 5nm $Ga_{0.95}Mn_{0.05}As$ Hall bars. $T = 20$ K. (b) AMR of a 5nm $Ga_{0.95}Mn_{0.05}As$ film in the Corbino geometry. (c) AMR for macroscopic Hall bars and (d) narrow (1 μm wide) Hall bars.

servation of the highly unconventional 6% AMR totally dominated by the uniaxial crystalline term.

The 5 nm films have lower Curie temperatures ($T_C \approx 30$ K) than the 25 nm films and become highly resistive at low temperature indicating that they are close to the metal-insulator transition. (The 25 nm films show metallic behavior down to the lowest measured temperatures.) The strength of the effect in the 5 nm films is remarkable and it is not captured by theory simulations assuming weakly disordered, fully delocalized (Ga,Mn)As valence bands. It might be related to the expectation that magnetic interactions become more anisotropic with increasing localization of the holes near their parent Mn ions as the metal-insulator transition is approached [14].

Finally, we demonstrate how the crystalline terms can be tuned by the use of lithographic patterning to induce an additional uniaxial anisotropy in narrow Hall bars. Recently [13], it has been found that the patterning allows the in-plane compressive strain in the (Ga,Mn)As film to relax in the direction along the width of the bar and this can lead to an additional uniaxial component in the magnetocrystalline anisotropy for bars with widths on the order of 1 μm or less. Figures 3(c) and 3(d) show the AMR of 45 μm and 1 μm wide bars fabricated from nominally identical 25 nm $Ga_{0.95}Mn_{0.05}As$ wafers. For the 45 μm bars, the cubic crystalline symmetry leads to the AMR along [100] and [010] being larger than along [110] and $[1\bar{1}0]$. For the narrow bars we observe the opposite relationship. This is consistent with the addition of an extra uniaxial component, whose presence in the magnetocrystalline anisotropy is confirmed by SQUID magnetometry measurements, which adds 0.8% to the AMR when current is along [110] and $[1\bar{1}0]$ and subtracts 0.4% when the current is along [100] and [010]. These postgrowth lithography induced modifications are significant fractions of the total AMR of the (Ga,Mn)As material.

To conclude, we have described the noncrystalline AMR in (Ga,Mn)As as a combined effect of the SO-coupled spin-texture in the host band and polarized scatterers containing nonmagnetic and magnetic impurity potentials. The crystalline terms are associated with band warping effects reflecting the underlying crystal symmetry. Our theory should apply to a large family of related dilute moment systems suggesting, e.g., that the noncrystalline AMR sign flips when the $\mathbf{s} \parallel \mathbf{k}$ Kohn-Luttinger spin texture is replaced by the $\mathbf{s} \perp \mathbf{k}$ Rashba-type SO coupling of asymmetric 2D systems, or when Mn forms an isovalent, pure magnetic impurity as in II-VI semiconductor structures. We have established a technique for direct measurement of the crystalline AMR components by utilizing the Corbino disk geometry, which should also be applicable to other systems which combine high crystalline quality with relatively high resistivity. In epitaxial ultrathin (Ga,Mn)As films the AMR is dominated by a large uniaxial crystalline component and in standard films the crystalline components can be modified by microscale lithography induced lattice relaxations.

We acknowledge collaborations with J. Chauhan, D. Taylor, K.Y. Wang, and M. Sawicki, and support from EU Grant IST-015728, from UK Grant GR/S81407/01, from CR Grants 202/05/0575, 202/04/1519, FON/06/E002, AV0Z1010052, and LC510, from ONR Grant N000140610122, and from SWAN. J. Sinova received additional support from the Research Corporation.

[1] W. Döring, Ann. Phys. (Leipzig) **424**, 259 (1938).
[2] R. P. van Gorkom, J. Caro, T.M. Klapwijk, and S. Radelaar, Phys. Rev. B**63**, 134432 (2001).
[3] J. Banhart and H. Ebert, Europhys. Lett. **32**, 517 (1995).
[4] T. McGuire and R. Potter, IEEE Trans. Magn. **11**, 1018 (1975);J. Smit, Physica (Amsterdam) **17**, 612 (1951).
[5] D. V. Baxter, *et al.*, Phys. Rev. B **65**, 212407 (2002).
[6] T. Jungwirth, *et al.*, Appl. Phys. Lett. **83**, 320 (2003).
[7] H. X. Tang, R. K. Kawakami, D. D. Awschalom, and M. L. Roukes, Phys. Rev. Lett. **90**, 107201 (2003).
[8] F. Matsukura, M. Sawicki, T. Dietl, D. Chiba, and H. Ohno, Physica (Amsterdam)**21E**, 1032 (2004).
[9] S. T. B. Goennenwein, *et al.*, Phys. Rev. B **71**, 193306 (2005).
[10] K. Y. Wang, *et al.*, Phys. Rev. B **72**, 085201 (2005).
[11] W. Limmer, *et al.*, Phys. Rev. B **74**, 205205 (2006).
[12] T. Jungwirth, M. Abolfath, J. Sinova, J. Kučera, and A. H. MacDonald, Appl. Phys. Lett. **81**, 4029 (2002).
[13] S. Hümpfner, *et al.*, Appl. Phys. Lett. **90**, 102102 (2007); J. Wunderlich, A. C. Irvine, J. Zemen, V. Holý, A. W. Rushforth, E. De Ranieri, U. Rana, K. Výborný, J. Sinova, C. T. Foxon, R. P. Campion, D. A. Williams, B. L. Gallagher, and T. Jungwirth, Phys. Rev. B **76**, 054424 (2007).
[14] T. Jungwirth, J. Sinova, J. Mašek, J. Kučera, and A. H. MacDonald, Rev. Mod. Phys. **78**, 809 (2006).
[15] T. Jungwirth, Jairo Sinova, A. H. MacDonald, B. L. Gallagher, V. Novák, K. W. Edmonds, A. W. Rushforth, R. P. Campion, C. T. Foxon, L. Eaves, E. Olejník, J. Mašek, S.-R. Eric Yang, J. Wunderlich, C. Gould, L. W. Molenkamp, T. Dietl, and H. Ohno, Phys. Rev. B **76**, 125206 (2007).
[16] T. Dietl, H. Ohno, and F. Matsukura, Phys. Rev. B **63**, 195205 (2001).
[17] T. Jungwirth, Q. Niu, and A. H. MacDonald, Phys. Rev. Lett. **88**, 207208 (2002).
[18] The microscopic origin of the uniaxial symmetry breaking mechanism in the (Ga,Mn)As epilayers is not known but is modeled by a weak in-plane shear strain [19].
[19] M. Sawicki, *et al.*, Phys. Rev. B **71**, 121302 (2005).
[20] Strictly, in the Corbino geometry we measure $G^C = I/V = (\sigma_{xx} + \sigma_{yy})/2$ and plot $R^C = 1/G^C$. However, since $\rho_{xy} \ll \rho_{xx}$ to a good approximation $\Delta R^C/R^C_{\rm av} = (\Delta R^H_{[110]} + \Delta R^H_{[1\bar{1}0]})/R^H_{\rm av} = C_U \cos(2\psi) + C_C \cos(4\psi)$, where the superscripts refer to Corbino and Hall bar measurements.
[21] A. W. Rushforth, *et al.*, Phys. Status Solidi C **3**, 4078 (2006).